Quantifying the influence of channel sinuosity on the depositional mechanics of channelized turbidity currents: A laboratory study

Kyle M. Straub [a,*], David Mohrig [b], James Buttles [b], Brandon McElroy [b], Carlos Pirmez [c]

[a] Department of Earth and Environmental Sciences, Tulane University, New Orleans, LA 70118, USA
[b] Department of Geological Sciences, The University of Texas at Austin, Austin, TX 78712, USA
[c] Shell International Exploration and Production Inc., P.O. Box 481, Houston, TX 77001, USA

ARTICLE INFO

ABSTRACT

Here we present results from a suite of laboratory experiments that highlight the influence of channel sinuosity on the depositional mechanics of channelized turbidity currents. We released turbidity currents into three channels in an experimental basin filled with water and monitored current properties and the evolution of topography via sedimentation. The three channels were similar in cross-sectional geometry but varied in sinuosity. Results from these experiments are used to constrain the run-up of channelized turbidity currents on the outer banks of moderate to high curvature channel bends. We find that a current is unlikely to remain contained within a channel when the kinetic energy of a flow exceeds the potential energy associated with an elevation gain equal to the channel relief; setting an effective upper limit for current velocity. Next we show that flow through bends induces a vertical mixing that redistributes suspended sediment back into the interiors of depositional turbidity currents. This mixing counteracts the natural tendency for suspended sediment concentration and grain size to stratify vertically, thereby reducing the rate at which sediment is lost from a current via deposition. Finally, the laboratory experiments suggest that turbidity currents might commonly separate from channel sidewalls along the inner banks of bends. In some cases, sedimentation rates and patterns within the resulting separation zones are sufficient to construct bar forms that are attached to the channel sidewalls and represent an important mechanism of submarine channel filling. These bar forms have inclined strata that might be mistaken for the deposits of point bars and internal levees, even though the formation mechanism and its implications to channel history are different.

Published by Elsevier Ltd.

1. Introduction

High resolution mapping of continental slopes has revealed ubiquitous channels (Clark et al., 1992; Demyttenaere et al., 2000; Droz et al., 1996; Flood and Damuth, 1987; Kenyon et al., 1995; Pirmez et al., 2000; Pratson et al., 1994; Schwenk et al., 2003), some extending in excess of 3000 km and into water depths exceeding 4000 m (Schwenk et al., 2003). These channels are primarily constructed by turbidity currents, mixtures of water and suspended sediment that move down continental margins as underflows. Turbidity currents dominate the transport of terrigenous sediment to deep-marine locations (Kneller and Buckee, 2000) and have built some of the largest sediment accumulations found on Earth (Bouma et al., 1985). These deposits host many of the largest producing petroleum reservoirs in the world today (Weimer and Link, 1991). In spite of this, our knowledge of

the system properties allowing for sediment in turbidity currents to be transported for great distances is incomplete. This limits our ability to both model the evolution of deep-marine stratigraphy and invert stratigraphic architecture observed in outcrop (Fildani et al., 2009; Romans et al., in this issue; Flint et al., 2011; Kane and Hodgson, 2011; Pyles, 2008) or seismic data (Abreu et al., 2003; Nakajima et al., 2009) for formative flow conditions. This deficiency is largely a consequence of difficulty in instrumenting natural flows due to the great water depth, infrequent occurrence, and high velocities associated with many turbidity currents. We argue here that furthering our understanding of the evolution of seascapes requires not only a refinement of internal turbidity current dynamics, but also a refinement in our knowledge of how interactions with seafloor topographies mediate the transport properties of turbidity currents. In particular we focus on the influence that channel sinuosity has on the depositional mechanics of turbidity currents.

Comparison of channelized terrains in terrestrial and submarine environments provides scientists with an opportunity to explore

* Corresponding author.
  E-mail address: kmstraub@tulane.edu (K.M. Straub).

the generality of landscape evolution models in settings with substantially different environmental conditions. To date most theory describing channel initiation and evolution has been tested for terrestrial conditions where the density (ρ_c) of the transporting flow is substantially greater than the ambient fluid density (ρ_a). For rivers and air on the Earth's surface, ρ_c/ρ_a is ~830. However, for turbidity currents this ratio is typically only 1.01–1.1 (Simpson, 1987). Expanding terrestrial theories that describe the interactions between fluid flow and channel development to environments with different ratios of ρ_c/ρ_a will help us interpret environmental settings on other planets and moons where channels have recently been discovered. For example, on Venus and Titan the ratio for channel-forming flows is thought to fall somewhere in between the terrestrial and submarine environments. Channels on Venus are hypothesized to be the result of either lava flows or sediment gravity flows (Bray et al., 2007; Williams-Jones et al., 1998). Given the high surface density of the Venus atmosphere, lava flows would have a ρ_c/ρ_a of ~ 32 and sediment gravity flows would have a ρ_c/ρ_a of 1.01–1.1. On Titan, ρ_c/ρ_a is expected to be ~75, an order of magnitude less than the value for terrestrial rivers as a result of the low density of liquid methane (Perron et al., 2006; Tomasko et al., 2005).

Published data on submarine channels reveals that many are moderately to highly sinuous (sinuosity > 1.2); including three of the four longest, the Bengal (Schwenk et al., 2003), Indus (Kenyon et al., 1995), and Amazon (Flood and Damuth, 1987) channels. These sinuous submarine channels share many planform characteristics with rivers, including comparable scaling relationships between channel widths and meander-bend wavelengths and amplitudes (Pirmez and Imran, 2003). In addition, the properties of long profiles for channels in both environments adjust in response to changes in sediment fluxes, liquid fluxes, and tectonic activity (Kneller, 2003; Pirmez et al., 2000). The similarities have been used to justify the adoption of models for subaerial channelized flow as semi-quantitative guides for interpreting flow through sinuous submarine channels even though significant differences exists between the two environments (Imran et al., 1999; Komar, 1969).

While many similarities in the morphodynamics of rivers and submarine channels exist, differences in the physics of the two systems also impart significant differences in their spatial and temporal evolution. In rivers, gravity acts on water which in turn drags sediment down slope. In submarine channels, gravity acts on the excess density associated with sediment suspended within the turbidity current which in turn drives the down slope flow. This difference in driving force substantially changes the down slope evolution of turbidity currents relative to rivers. For example, some river systems evolve to a state where their slope, channel depth, width, planform and roughness are mutually adjusted in response to changes in flow discharge and sediment discharge to transport all sediment load through a system without aggradation or degradation of the channel (Mackin, 1948). This situation leads to an equilibrium profile for rivers in which the channel-forming flow in the alluvial section of the profile is at capacity with the local sediment transport limit (Howard, 1980). This situation does not occur in the medial and distal segments of most submarine channel systems where the topography and the currents constructing it are clearly net depositional (Babonneau et al., 2002; Pirmez et al., 2000; Pirmez and Imran, 2003). The work presented in this study is most applicable to the mid to distal ends of submarine channel systems that are net depositional.

During the past decade multiple studies have compared the interactions of river flows and turbidity currents with channel bends (Abreu et al., 2003; Corney et al., 2006; Das et al., 2004; Imran et al., 2007, 1999; Islam et al., 2008; Kane et al., 2008; Kassem and Imran, 2005; Peakall et al., 2007, 2000; Pirmez and Imran, 2003; Straub et al., 2008). These studies have utilized 3-D

seismic data, laboratory experiments, and numerical models to highlight both similarities and differences in fluid dynamics and sediment transport in the two environments. While much work on this subject has been performed, several fundamental questions still exist, some of which we hope to address in this manuscript. For example, how does the interaction of turbidity currents with channel bends affect their sediment transport capacity and what constraints can we place on the velocity of turbidity currents in sinuous channels. Here we address these and other issues related to turbidity current-channel bend interactions using reduced scale laboratory experiments. Due to a lack of direct measurements of the interactions of currents with submarine channels in the field, physical experiments have played a critical role in testing the intuition we have regarding these processes derived from fluvial systems (Metivier et al., 2005; Mohrig and Buttles, 2007; Straub et al., 2008). In addition, they provide the community with dynamic measurements to test numerical models against (Kassem and Imran, 2005; Sylvester et al., 2011; McHargue et al., in this issue). We released sequences of depositional turbidity currents into three channels. These channels shared a similar cross-sectional geometry but varied in sinuosity. Where possible, we examine how our observations might also inform studies of current-channel interactions in extraterrestrial environments.

2. Experimetal setup

We released density currents into a basin 5 m long, 5 m wide, and 1.2 m deep, that remained filled with water throughout each experiment (Fig. 1). Five experiments were performed in the basin. For experiments 1, 2, and 3, sequences of sediment laden turbidity currents were released into channels with sinuosities of 1.00 (straight), 1.04 (low sinuosity), and 1.32 (high sinuosity). In these three experiments the initial conditions were held constant for each turbidity current in order to isolate the effect of sinuosity on deposition in submarine channels (Table 1). Before filling the basin with water at the start of each experiment, a channel was built on the basin floor. The planform geometry for the three channels was designed using a sine-generated curve which has been shown to reproduce the shapes of many subaerial and subaqueous channels (Langbein and Leopold, 1966; Pirmez, 1994). This curve describes the local direction of the channel centerline, φ, as a function of streamwise distance, x:

$$\varphi = \omega \, \sin \frac{x}{X_t 2\pi} \tag{1}$$

Where ω is the maximum angle at which the centerline deviates from the mean downstream direction and X_t is the centerline distance associated with one channel wavelength. Parameters used to design the planform shape of the three channel types are listed in Table 2 and their initial morphologies are displayed in Figs. 2, 3 and 4. Channel sidewalls and banks were constructed from a 15:1 mixture of sand and cement mortar. The initial cross-sections for the three channels were trapezoidal in shape. The straight and high sinuosity channels had initial depths of 0.11 m and basal and top widths of 0.20 m and 0.40 m, while the low sinuosity channel had an initial depth of 0.08 m and basal and top widths of 0.10 m and 0.515 m. The three channels were built with no initial downstream bed slope. After traversing the channels each current spread out onto a short unconfined surface before plunging into a moat where it was removed from the basin via perforated pipes, thereby preventing current reflections off of tank sidewalls.

The turbidity currents released in experiments 1–3 were composed of the same mixture of clear water, dissolved $CaCl_2$ and suspended sediment. This mixture produced currents that entered

A Plan View

B Side View
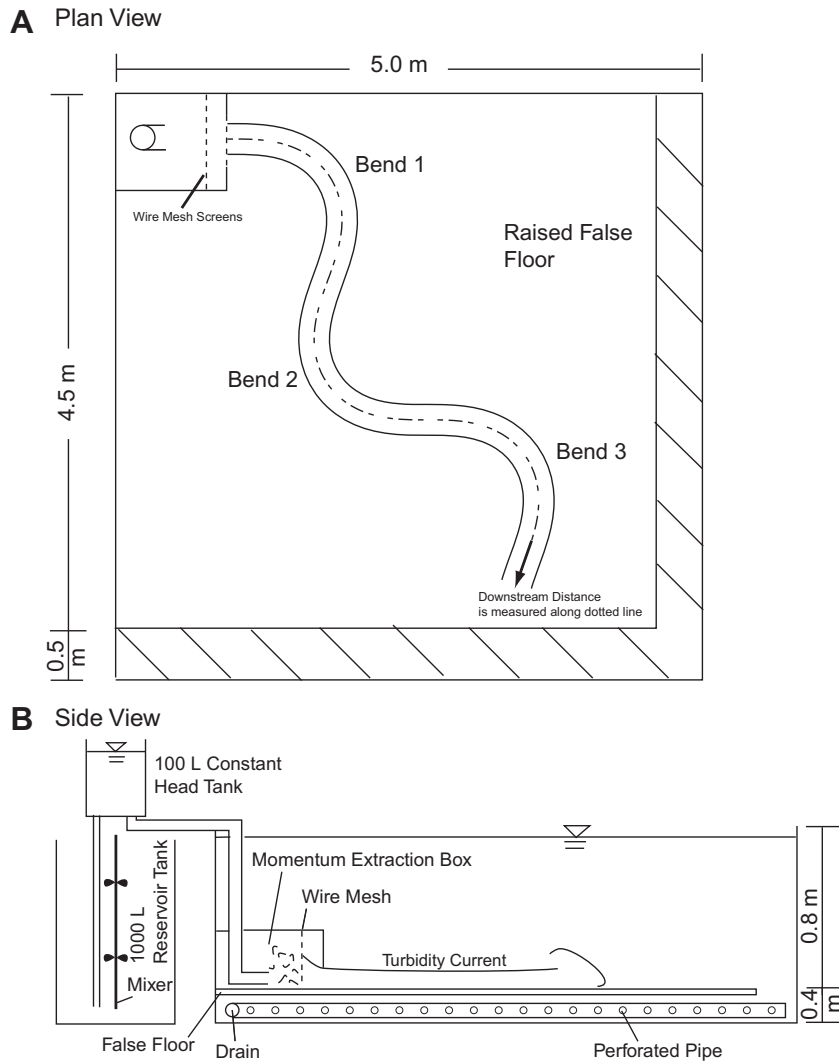
Fig. 1. Schematic diagram of the experimental facility. (A) Planform view of the basin and an initial channel form. Each current passed through a momentum extraction box located in the top left basin corner prior to entering the channel. Diagonal lines mark the position of a moat for collecting a current following its passage through the channel, avoiding reflections off of tank walls. (B) Side view of the facility. Each current is mixed in a reservoir tank and pumped up into a constant head tank before entering the basin.

the channel with an absolute density of 1021 kg/m³ and an excess density of 2.1% relative to the fresh water that filled the basin. Of this excess density, 33% was due to suspended sediment and 67% was from the dissolved salt. The sediment consisted of 60% blown silica (ballotini) and 40% crushed silica flour by weight with a cumulative size distribution where D1, D5, D10, D16, D25, D50, D75, D84, D90, D95, and D99 equaled nominal diameters of 1.7 μm, 3.1 μm, 12.9 μm, 18 μm, 23 μm, 31 μm, 41 μm, 46 μm, 52 μm, 60 μm,

and 80 μm, respectively (Fig. 5). Dissolved salt was used to simulate the finest portion of suspended sediment within natural turbidity currents, a fraction that is transported to the distal end of a system without loss via deposition and is well mixed vertically within the turbidity currents. The mixture of water, sediment, and dissolved salt was introduced to the basin via a constant head tank that guaranteed steady input discharge throughout each individual release. Each current passed through a momentum extraction box

Table 1
Flow characteristics of experimental turbidity currents.

Experiment #	Channel sinuosity	Flow #	u_{in} (m/s)	H (m)	ρ_c (kg/m³)	T (hr)	Fr	Re
1	1	1–10	0.13	0.11	1021	8.8×10^{-2}	0.86	14 300
2	1.04	1–27	0.12	0.11	1021	1.5×10^{-1}	0.80	13 200
3	1.32	1–24	0.08	0.12	1021	8.8×10^{-2}	0.51	9600
4	1.04	1	0.05	0.11	1030	8.8×10^{-2}	0.29	5720
4	1.04	2	0.13	0.11	1030	1.5×10^{-1}	0.72	14 300
5	1.32	1	0.07	0.1	1004	9.9×10^{-2}	1.07	6700
5	1.32	2	0.04	0.1	1004	9.6×10^{-2}	0.70	4400
5	1.32	3	0.07	0.1	1034	8.4×10^{-2}	0.38	6900
5	1.32	4	0.06	0.1	1034	9.4×10^{-2}	0.35	6300
5	1.32	5	0.08	0.1	1034	8.8×10^{-2}	0.42	7700
5	1.32	6	0.09	0.1	1021	8.3×10^{-2}	0.62	8900

Table 2
Parameters used to design the planform shape of experimental channels.

	Straight channel	Low sinuosity channel	High sinuosity channel
Sinuosity	1	1.04	1.32
ω	0	25^{0}	55^{0}
X_t	N/A	2.34 m	3.4 m
λ	Infinity	2.25 m	2.513 m
a	Infinity	0.285 m	0.39 m
r_0	Infinity	1.45 m	0.63 m

before entering the basin. This box was 0.5 m by 0.5 m in planform and contained several vertical screens of 5 mm wire mesh through which currents passed prior to entering the experimental channels. The momentum extraction box ensured that each flow acted as a sediment laden plume driven by buoyancy alone (see Supplementary Information for further discussion of experimental setup, scaling, and measurement techniques). Current thickness and discharge at the channel entrance was held constant for all flows released in experiment 1 (straight channel) and experiment 3 (high sinuosity channel) at values of 0.11 m and 4.7×10^{-3} m^3/s. All flows released in experiment 2 (low sinuosity channel) had a current thickness and discharge, measured at the channel entrance, of 0.11 m and 2.5×10^{-3} m^3/s, respectively.

Representative input values for the densimetric Froude number ($Fr = \overline{u}/\sqrt{[(\rho_c/\rho_a) - 1]gH}$), Reynolds number (Re $= \overline{u}H/v$), and buoyancy flux ($B_{f0} = \Delta\rho guHb/\rho$) during experiment 3 were 0.53, 8.2×10^3 and 5.3×10^{-4} m^4/s^3, respectively, where $\overline{u}$ is depth averaged velocity, ρ_c is current density, ρ_a is the ambient fluid density, g is gravitational acceleration, H is current thickness, v is kinematic viscosity, and b is mean channel width. The duration of currents in experiments 1, 2 and 3 were 5.3, 9.5, and 5.3 min, respectively.

In experiments 4 and 5, turbidity currents with varying input discharge and excess density were released into the low and high sinuosity channels. Experiments 4 and 5 were performed in order to quantify conditions under which currents traversing sinuous channels remain partially or completely channelized. Table 1 list input conditions for all flows released in these experiments.

Measurements of current velocity were collected using two Sontek Acoustic Doppler Velocimeters (ADV) and one Sontek Pulse-Coherent Acoustic Doppler Velocity Profiler (PCADP). An ADV was positioned at the channel entrance and exit for each turbidity current release. These devices recorded the 3-D velocity in a 2×10^{-7} m^3 sampling volume located 50 mm above the channel bed at the channel centerline with a frequency of 10 Hz. Vertical profiles of velocity were measured at many locations inside the channel using only one of the three transducers on the PCADP. During several flow events the PCADP was systematically moved
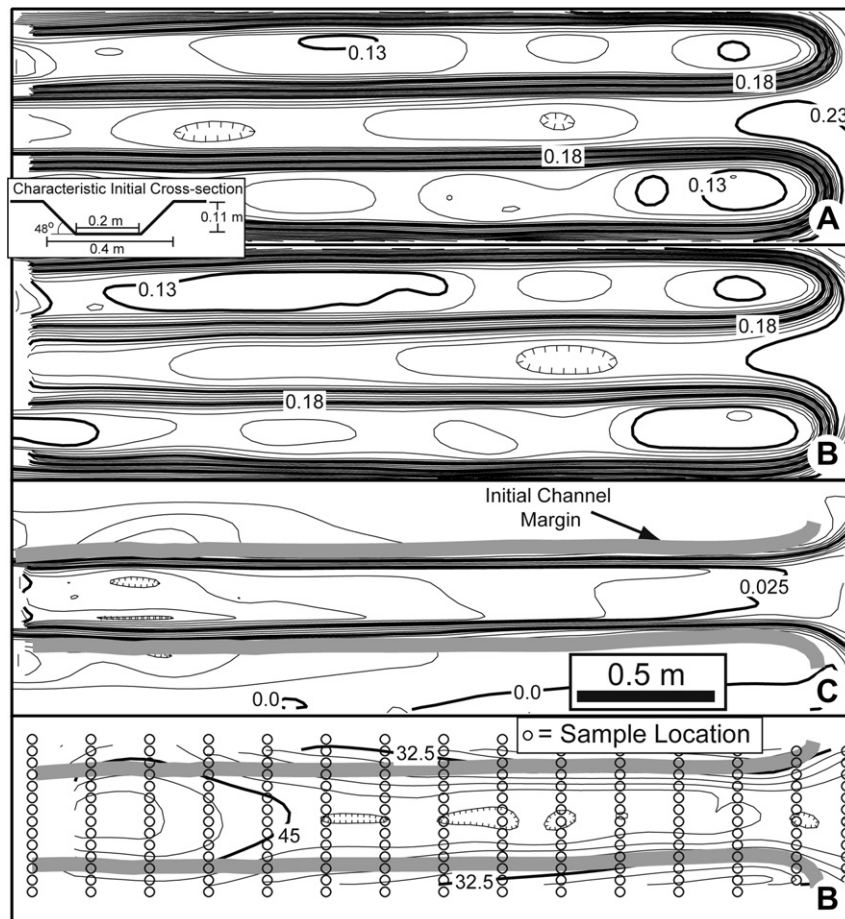
Fig. 2. Maps from the straight channel experiment (experiment 1). Channel flow was from the left to the right in each map. (A) Topographic map of the initial channel form. Topography is defined as vertical distance between the bed and an overlying datum of constant elevation. Contour interval is 5 mm. The inset depicts the average initial channel cross-section. (B) Topographic map of the final channel form following sedimentation by 10 currents. Contour interval is 5 mm. (C) Map of deposit thickness from sedimentation by 10 turbidity currents. This map is the difference between maps A and B. Contour interval is 2.5 mm. Gray bold lines represent location of channel margin prior to deposition by flow 1. (D) Map of nominal diameter associated with the median particle size for the local deposit. Contour interval is 2.5 μm. Circles mark the locations where vertically integrated sediment samples were collected for particle size analysis.
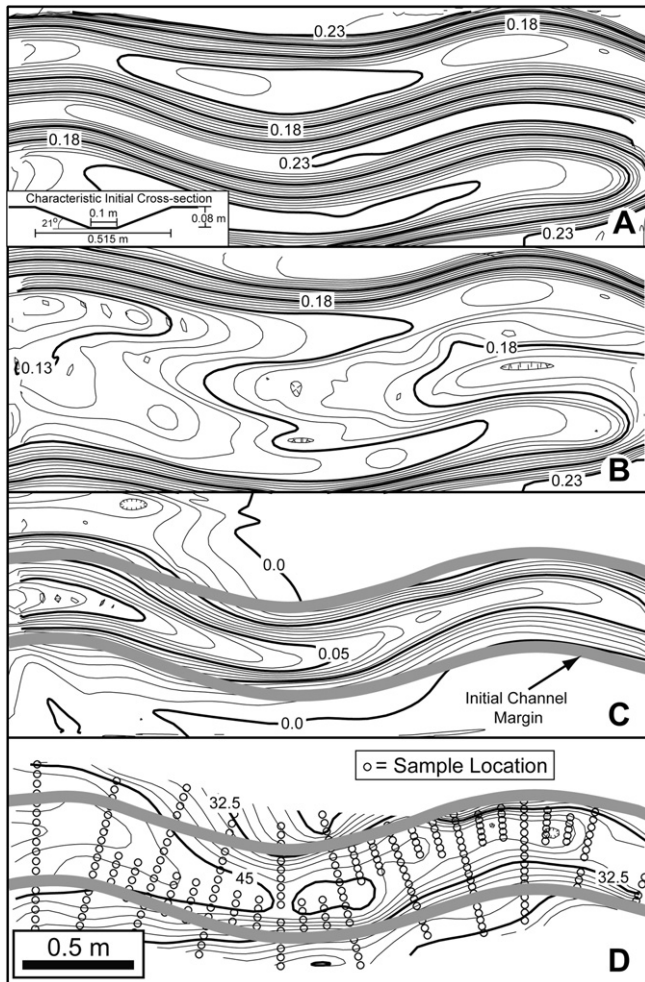
Fig. 3. Maps from the low sinuosity channel experiment (experiment 2). Channel flow was from the left to right in each map. (A) Topographic map of the initial channel form. Topography is defined as vertical distance between the bed and an overlying datum of constant elevation. Contour interval is 5 mm. The inset depicts the average initial channel cross-section. (B) Topographic map of the final channel form following sedimentation by 10 currents. Contour interval is 5 mm. (C) Map of deposit thickness from sedimentation by 27 turbidity currents. This map is the difference between maps A and B. Contour interval is 2.5 mm. Gray bold lines represent location of channel margin prior to deposition by flow 1. (D) Map of nominal diameter associated with the median particle size for the local deposit. Contour interval is 2.5 μm. Circles mark the locations where vertically integrated sediment samples were collected for particle size analysis.

from one channel bank to the opposite channel bank along a path perpendicular to the channel centerline to produce a cross-section of downstream velocity. The PCADP measured velocity with a frequency of 0.25 Hz in roughly cylindrical sampling volumes that were 1.6×10^{-2} m deep and had a horizontal footprint that varied in diameter from 7.1×10^{-2} m to 8.7×10^{-2} m with increasing distance from the transducer.

Suspended sediment profiles were collected during experiments 1 and 3 using a system of stacked siphons. Three siphons were deployed at various heights above the channel bed during successive flow events to produce profiles of concentration and median suspended sediment particle diameter. The 5 mm diameter siphons were positioned over the channel centerlines facing upstream, 2.95 m from the channel entrance and drew roughly 600 mL of current into the sample bottles located outside of the basin. Siphons were opened following passage of the current head and remained open until 600 mL of fluid was collected. Siphons were positioned at specified heights above the channel bed prior to a flow event and

then remained fixed in position during the next flow event. Corrections of measured concentrations were made to account for a slight difference between velocity of flow through siphon and mean flow velocity (Anderson, 1941). The suspended sediment samples were analyzed for grain size with a Horiba LA-300 laser-particle size analyzer (LPSA). The LPSA uses a diode laser to accurately measure a distribution of sizes ranging from 0.001 to 0.3 mm in diameter.

Maps of channel form following each turbidity current release were produced using a submerged 1 KHz long range displacement laser connected to a data logger for experiments 1, 2, and 4 and using the first hard returns from a 1 MHz ultrasonic transducer connected to a pulse/receiver box for experiments 3 and 5. Bathymetric maps in experiments 1, 2, and 4 were collected on a grid with a 2 mm cross-stream spacing and 5 mm downstream spacing. Bathymetric maps in experiments 3 and 5 were collected on a grid with a 5 mm cross-stream spacing and 40 mm downstream spacing. The vertical precision at each location for all experiments is better than 0.2 mm. This resolution makes it possible to successfully determine the patterns of sediment deposition associated with individual currents by differencing successive maps of channel topography. Topographic surveys were designed to capture most of the sedimentation that occurred in the basin resulting from the release of each turbidity current. As such, the cross-stream extent of each survey was set at a width suitable to capture sedimentation in excess of 0.5 mm per flow event. This mapping strategy allows us to quantify the total volume of sediment deposited from each turbidity current release as a function of distance from the source.

Overhead video was collected throughout the duration of each current. These movies recorded passage of the head of the current through each channel. The structure of the flow field associated with the body of each current was imaged by releasing a 15 mL pulse of dye at the channel entrance about 2 min following the start of each flow. These dye pulses were captured on the overhead video and maps of dye-front position through time were used to define the magnitude and direction of maximum horizontal velocity throughout the coupled channel-overbank flow field.

Following the end of experiments 1, 2, and 3 the water level in the experimental basin was lowered, and the deposits were allowed to dry. After drying, the deposits were sampled for particle size characterization using the same LPSA used for particle size analysis of the suspended sediment samples.

A comparison of our experiments to the morphodynamics of natural submarine channels can be achieved through classic dynamic scaling methods. We follow the methods presented in Straub et al. (2008) to estimate the flow and sediment transport regimes that our experiments best resemble at field scale. Below we describe how conditions corresponding to experiment 1 relate to field conditions, further information describing the scaling of experiments 2–5 can be found in the Supplementary Information. Upscaling here is performed using a geometric scaling of 1:1000 between the laboratory and the field environment. This scale factor results in maximum width, depth, and length scales of 400 m, 110 m, and 3 km. Current properties can be compared using three dimensionless parameters, Fr, the ratio of particle fall velocity to the shear velocity, w_s/u^*, and Re. An approximate dynamic similarity between the model and a natural system is ensured by setting $Fr_{(model)} = Fr_{(prototype)}$ (Graf, 1971). This equality in densimetric Froude number is satisfied by prototype values of u_x, H and current duration of 4.1 m/s, 110 m, and 2.7 h. Sediment transporting conditions were upscaled by setting $w_s/u^*_{(model)} = w_s/u^*_{(prototype)}$. w_s was calculated using the method from Deitrich (1982). $u^*_{(model)}$ was estimated at $5.2 \pm 0.8 \times 10^{-2}$ m/s for experiment 1 by fitting the equation:

$$u(z) = \frac{u^*}{\kappa}\ln\left(\frac{z}{z_0}\right) \quad (2)$$
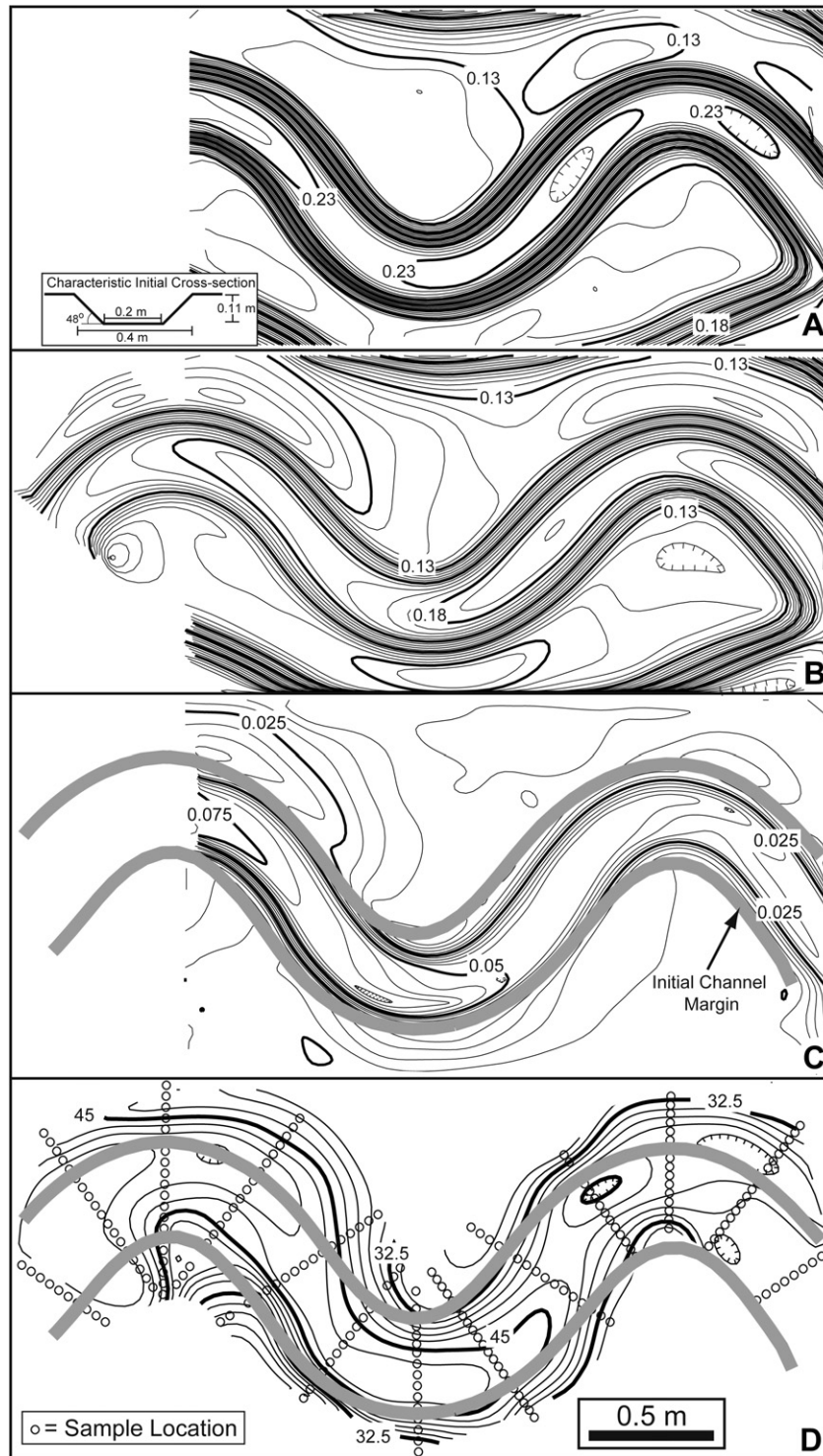
Fig. 4. Maps from the high sinuosity channel experiment (experiment 3). Channel flow was from the left to the right in each map. (A) Topographic map of the initial channel form. Topography is defined as vertical distance between the bed and an overlying datum of constant elevation. Contour interval is 5 mm. The inset depicts the average initial channel cross-section. (B) Topographic map of the final channel form following sedimentation by 24 currents. Contour interval is 5 mm. (C) Map of deposit thickness from sedimentation by 24 turbidity currents. This map is the difference between maps A and B. Contour interval is 2.5 mm. Gray bold lines represent location of channel margin prior to deposition by flow 1. (D) Map of nominal diameter associated with the median particle size for the local deposit. Contour interval is 2.5 μm. Circles mark the locations where vertically integrated sediment samples were collected for particle size analysis.

to velocity data collected with the PCADP (see Supplementary Information), where κ is von Karman's constant and is equal to 0.4, and z_0 is a roughness parameter, equal to the elevation at which the extrapolated logarithmic velocity profile goes to zero. $u^*_{(prototype)}$ was estimated using the equation:

$$u^* = \sqrt{C_f}\, \bar{u} \qquad (3)$$

where C_f is a dimensionless friction coefficient that has been estimated for field scale turbidity currents to be approximately 2×10^{-3} (Garcia, 1994; Parker et al., 1987) and $\bar{u}_{(prototype)}$ is set to
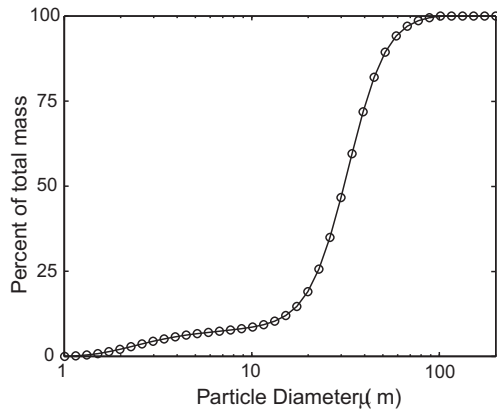
Fig. 5. Particle size distribution for the sediment discharged into experimental basin.

the value estimated from the earlier Froude scaling. Resulting values for D5, D50, and D95 in the prototype system were 25 μm, 111 μm, and 255 μm. While our intention was not to produce an analogue model of any one submarine channel setting, we do note that the prototype geometric, flow, and sediment transport properties of our experiments compare favorably to properties of the Amazon submarine channel system (Pirmez and Imran, 2003). Finally, $Re_{(model)}$ was sufficiently large to satisfy the approximate Reynolds similarity for fully turbulent gravity currents proposed by Parsons and Garcia (1998).

3. Experimental results

The experiments summarized in this study had three primary goals, 1) characterize how channel sinuosity effects sedimentation patterns of depositional flows, 2) characterize how channel bends of varying curvature effect flow properties, and 3) constrain the maximum flow velocity for turbidity currents in sinuous channels. The depositional nature of all sediment laden density currents released into the study channels resulted in deposits that were thickest at the channel entrance and systematically thinned with increasing downstream distance. In addition, deposit particles were coarsest at the channel entrance and fined in size with increasing distance from the source. Superimposed on these downstream trends in deposit thickness and particle size are cross-stream trends that record the influence of channel bends on sediment transport and deposition. We begin by documenting these deposition patterns in experiments 1−3.

3.1. Deposition connected with flow through a straight channel (experiment 1)

Ten turbidity currents were released into the straight channel during experiment 1. Each current had identical input conditions for current thickness, discharge, and excess density. These turbidity currents produced a tapered deposit that decreased in thickness and grain size with distance down the channel centerline. Using isopach maps which record the magnitude of deposition between two successive flow events we found that each flow deposited 4 ± 0.5 mm of sediment at the channel entrance and 2.5 ± 0.4 mm of sediment at the distal end of the channel. The stacking of tapered deposits generated a centerline bed slope that was 5×10^{-3} m/m after the release of the tenth flow (Fig. 2B). Cross-channel deposition on the bed was relatively constant at any position down the channel with only minor local variability connected to minor irregularities in original channel bottom form (Fig. 2C). Trends in

particle size for the deposit mimicked deposit thickness trends (Fig. 2D). The median particle size deposited at the channel entrance was 50 μm and fined to 43 μm at the distal end of the channel centerline. The median particle size was approximately constant on any cross-channel transect of the channel floor.

Sediment deposition was not limited to the bed of the channel, but also occurred on the channel sidewalls and in the overbank environment. Sediment initially deposited on the steep sidewalls via suspension fallout was always unstable and remobilized by currents into grain flows that accumulated at the base of the sidewalls on the channel floor. The resulting sediment wedges had a maximum surface angle of 21°, close to the particle angle of repose when subjected to lateral shear stresses by overriding turbidity currents. Sedimentation on the overbank produced topographic levees. Overbank deposition was always greatest at the channel margin and decreased with distance from the channel bank line. Every overbank deposit was thinner and finer grained than its laterally adjacent channelized deposit.

3.2. Deposition by flow through a low sinuosity channel (experiment 2)

Evolution of channel topography in experiment 2 was associated with the release of 27 strongly depositional turbidity currents. Similar to experiment 1, each current had identical input conditions and each current resulted in a deposit that decreased in thickness and median grain size with distance from the channel entrance along its centerline. Each flow deposited 3.5 ± 0.5 mm of sediment at the channel entrance and 1.5 ± 0.3 mm of sediment at the distal end of the channel. Following the release of the 27 currents the deposit had an average bed slope along the channel centerline of 1.8×10^{-2} m/m. Along the channel centerline the median deposit particle size decreased from 52 μm at the channel entrance to 38 μm at the distal end of the channel. The channelized deposit was reworked into trains of ripples that extended the entire channel length (Fig. 6). These ripples had amplitudes between 0 and 5 mm and wavelengths between 50 and 100 mm. Superimposed on the basic downstream trends are systematic, cross-channel variations in deposit thickness and accompanying particle size (Fig. 7). In every bend the location of the thickest and coarsest-grain deposit was always displaced laterally from the centerline of the channel toward the outer bank. Prominent bar topography developed along the inner bank beginning immediately downstream from the apexes of bends 1 and 2 (Figs.3B, 6C, and 7). The growth of these bars occurred during deposition by all 27 turbidity currents and is distinct from other channel deposits in that their surfaces were not reworked into ripples. Unlike experiment 1, the initial channel sidewall slopes in this experiment were 21° and allowed for sediment aggradation via suspension fallout without subsequent failure as grain flows. Deposition on the overbank surface resulted in focused levee growth along the outer and inner banks of channel bend 1. Overbank deposits were thicker and coarser on the outer bend bank relative the inner bank. These deposits thinned with increasing distance from the channel and reached negligible thickness close to the apex of the second channel bend.

### 3.3. Deposition associated with flow through a high sinuosity channel (experiment 3)

Experiment 3 involved the release of 24 depositional turbidity currents into a channel with an original sinuosity of 1.32. Each flow deposited 3.5 ± 0.4 mm of sediment at the channel entrance and 1.2 ± 0.2 mm of sediment in the center of the channel at its distal end. Following the release of the 24 currents the deposit had an average bed slope along the channel centerline of 1.4×10^{-2} m/m
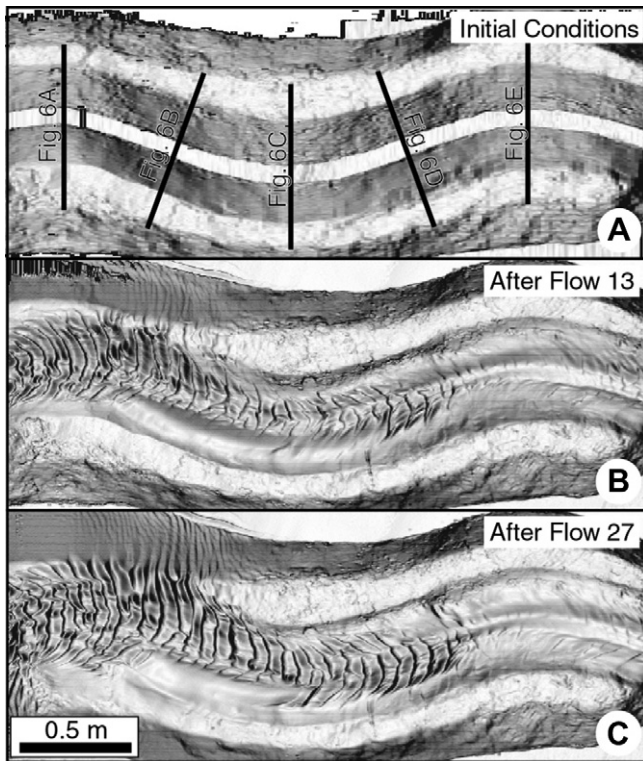
Fig. 6. Slope magnitude maps for evolving channel topography associated with the low sinuosity channel experiment (experiment 2) for the initial channel topography (A), topography following flow 13 (B), and topography following flow 27 (C). These slope maps were created by calculating the average absolute value for the local surface slope based on the surface elevations at each data bin and its eight immediate neighbors. High values of surface slope defining channel walls have high gray-scale intensities (appear dark colored). Locations for topographic cross-sections presented in Fig. 7 are identified.

Fig. 7. Evolution of channel cross-sections located at the apexs of the first (A), second (C), and third (E) channel bends in addition to the channel inflection points located between the first and second channel bend (B) and the second and third channel bend (D). Each figure displays the original channel form plus successive forms following sedimentation by two currents. All cross-sections are oriented perpendicular to the local centerline direction and oriented looking downstream.

(Fig. 4B,C). Similar to the first two experiments, the downstream trend in median particle size mimicked the deposit thickness trend (Fig. 4D). Along the channel centerline the median particle size for the deposit decreased from 53 μm at the channel entrance to 39 μm at the distal end of the channel. The surface of the deposit following the release of the 24th flow event was primarily smooth with ripples covering only 5% of the deposit area. Similar to experiment 2, systematic cross-channel variations in deposit thickness and particle size were superimposed on the down channel trends. In every bend the location of the thickest and coarsest-grain deposit was always displaced laterally from the centerline of the channel. In contrast to depositional patterns in experiment 2, inner bank locations downstream of the first, second, and third bends were sites of minimum in channel deposition associated with fine-grain sediment. Similar to experiment 1, sediment deposited on channel sidewalls was unstable due to high initial channel sidewall slopes and was remobilized as grain flows. These failures continued until the sidewall slope had been completely regraded to a new slope of ~21°. This regrading of the sidewall slopes systematically reduced the width of the channel bottom.

Straub et al. (2008) document significant run-up of currents onto the outer banks of channel bends in this experiment. A portion of this current was able to exit the channel and move onto the overbank surface, resulting in a pronounced asymmetry in overbank deposit properties. The run-up and overspill of currents at the outer banks of bends produced thick and coarse, wedge-like overbank deposits. In comparison, overbank deposits at the inner banks of channel bends were thinner, finer grained and had lower deposit tapers. In this experiment, the run-up of currents onto the outer banks of channel
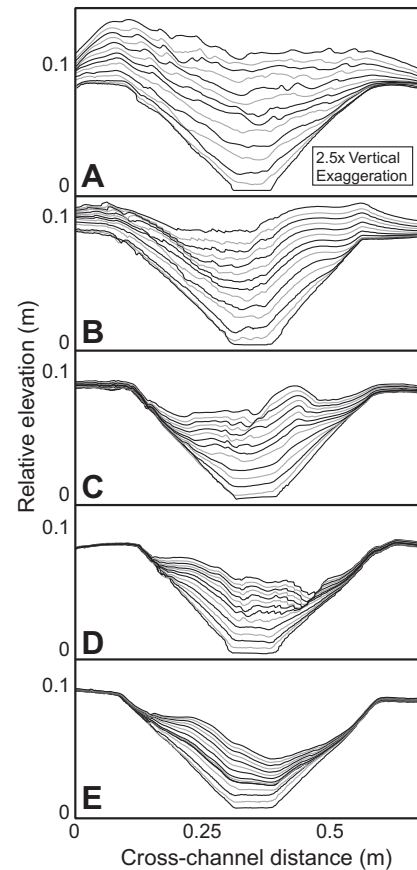
bends was so extreme that proximal overbank deposits shared the same distribution of particle sizes deposited on the channel bed.

3.4. Flow velocity data

Experiments 2–5 document varying degrees of containment for turbidity currents traversing sinuous channels. In order to estimate the control of flow and channel topography on this containment of currents we monitored current velocity using an ADV placed at the channel entrance and exit during all flows in experiments 2–5 (Table 1). Fully contained currents are associated with measures for the ratio of current velocity at the channel exit divided by current velocity at the channel entrance, (U_{out}/U_{in}), close to unity while weakly contained currents have measures for the ratio that are significantly smaller than one. We monitored how U_{out}/U_{in} varied as a function of the kinetic energy for a current, KE, relative to the potential energy associated with an elevation gain equal to the channel relief at a bend apex, PE. We define KE as:

$$KE = \frac{1}{2}\rho_c u^2 \tag{4}$$
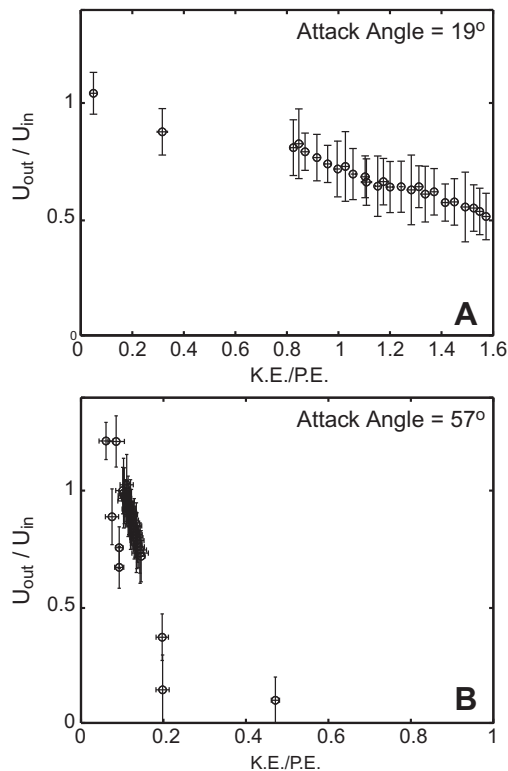
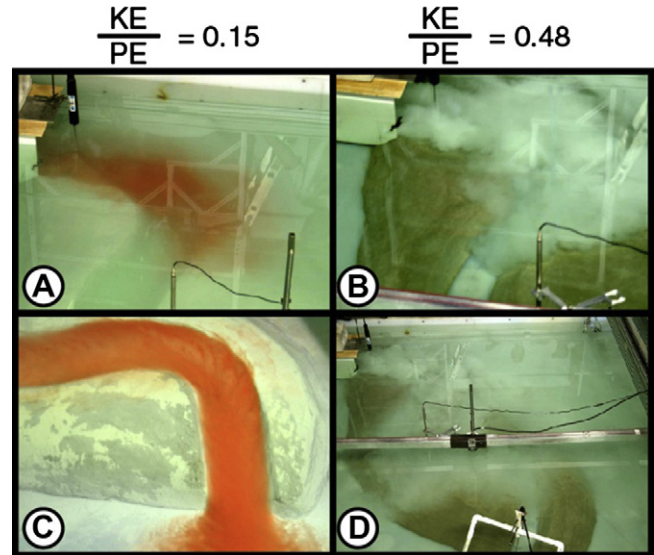and PE as:

$$PE = (\rho_c - \rho_a)gh \tag{5}$$

where h is defined here as the relief between the channel centerline and outer bank levee crest at the apex of the first channel bend at

the start of the flow event in question. In Fig. 8A we display how U_{out}/U_{in} varied as a function of KE/PE for flows through the low sinuosity channel used in experiments 2 and 4. Data from the channel of low sinuosity shows a gradual reduction in U_{out}/U_{in} from a value of ~1.0 for when KE/PE was 0.05 to a value for U_{out}/U_{in} of 0.55 when KE/PE increased to 1.6. This relatively gradual change in U_{out}/U_{in} for conditions in the low sinuosity channel was markedly different from the change observed in the high sinuosity channel. A more rapid decrease in U_{out}/U_{in} was noted for flows through the high sinuosity channel in experiments 3 and 5 (Fig. 8B). Values of U_{out}/U_{in} decreased from~1.1 to 0.2 while KE/PE increased from 0.05 to 0.2. Above a KE/PE value of 0.2, U_{out}/U_{in} only slowly decreased with further increases in KE/PE. Photographs of turbidity currents with KE/PE values of 0.15 and 0.48 are shown interacting with bends of the high sinuosity channel in Fig. 9.

The average path of the high-velocity core for turbidity currents was measured in experiments 1—3 using overhead digital video of dye pulses injected into the body of flows. For each current injected with dye, the location of the leading edge of a dye pulse was digitized every half second from the time of dye release until the dye-front reached the channel exit. The location of the fastest flow defined by maximum displacement of the leading edge of the dye pulse was measured for all currents and this data was assembled to produce a single map defining the position of the high-velocity core for each experiment. A comparison of the high-velocity core paths in experiments 1—3 is shown in Fig. 10. In experiment 1 the high-velocity core approximately followed the channel centerline over the full length of the straight channel. In experiment 2 the path of the high-velocity core does not follow the channel centerline, but is roughly an eighth of a wavelength out of phase with the centerline for this low sinuosity channel (Fig. 10B). The high-velocity core crosses the channel centerline roughly 0.3 m downstream of the

Fig. 9. Turbidity currents interacting with high sinuosity channel. Currents attack channel bends at an angle of 57°. Images (A) and (B) show low and high KE/PE currents, respectively interacting with channel near basin entrance point. Images (C) and (D) show low and high KE/PE currents, respectively, interacting with channel near basin exit point. Red color of flow in images (A) and (C) is result of dye added to flow body to aid visualization (For interpretation of the references to color in this figure legend, the reader is referred to the web version of this article).

apexes of bends 2 and 3. Maximum lateral separation between the position of the high-velocity core and the channel centerline occurs approximately at the inflection point between each of the channel bends. As in experiment 2, the path of the high-velocity core in experiment 3 is out of phase with the channel centerline (Fig. 10C). In this experiment the high-velocity core crosses the channel centerline a short distance upstream from the apexes of bends 1, 2, and 3 and maximum lateral separation between the high-velocity core and the channel centerline occurs slightly downstream from the apexes of the three bends.

To confirm that the location of the velocity maximum could be accurately determined using overhead photography and to gain more information on the cross-stream structure of the velocity field, several cross-sections of downstream velocity were collected with
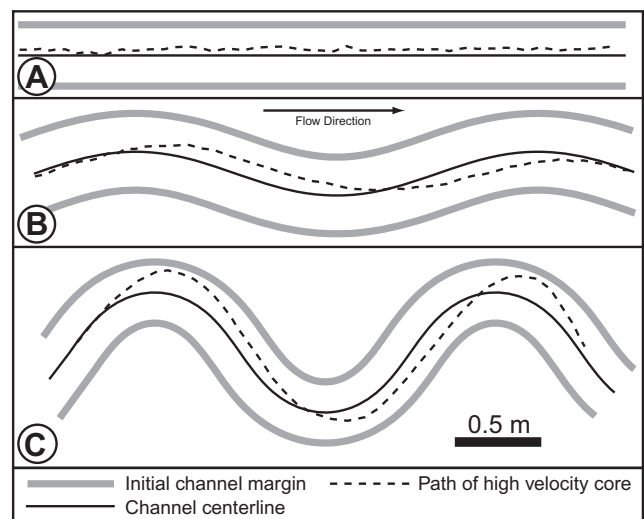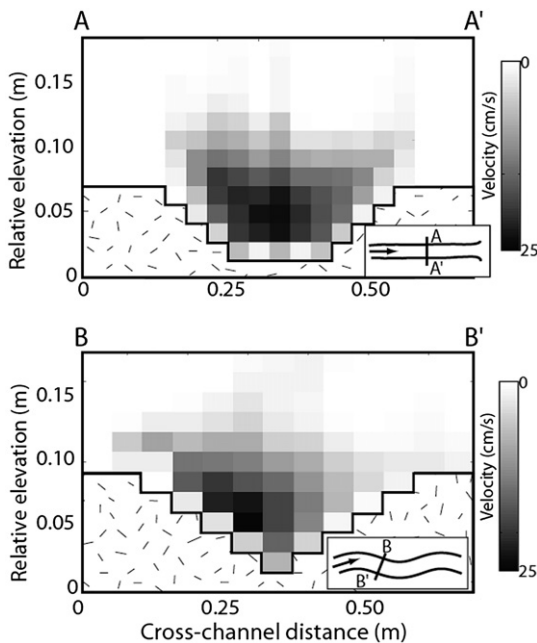

Fig. 8. Change in the ratio of U_{out}/U_{in} as a function of the ratio of KE/PE for experimental flows approaching the first bend of the low sinuosity channel (A) and the high sinuosity channel (B). Horizontal and vertical error bars represent plus and minus one standard deviation of measurement values.
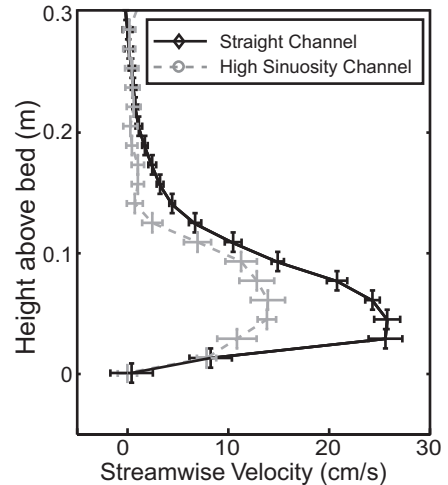

Fig. 10. Downstream paths of high-velocity core compared to the channel centerline for the straight channel (A), low sinuosity channel (B), and high sinuosity (C) channel experiments.

the PCADP. During the ninth current of experiment 1 a series of PCADP profiles were collected at 2.0 m from the channel entrance in order to produce a cross-section for the component of the velocity field oriented perpendicular to the channel centerline (Fig. 11A). In this cross-section the maximum downstream velocity occurs over the channel centerline, as estimated from the overhead photography. During the ninth current in experiment 2 a similar velocity cross-section was obtained for the component of the velocity field oriented perpendicular to the channel centerline at the inflection point between bends 1 and 2 (Fig. 11B). In this cross-section the high-velocity core is displaced from the channel centerline approximately 0.06 m toward the left-hand bank of the channel when looking downstream. This measured velocity displacement approximately coincides with the location of the velocity maximum mapped from overhead photography (Fig. 10B). Additionally, a strong cross-channel gradient in velocity and significant superelevation of the current toward the left-hand side of the channel is noted.

In order to quantify the drag associated with channel sinuosity we collected velocity profiles at the center of the channel 2.95 m from its entrance during experiments 1 and 3. This location corresponds to the inflection point between bends 2 and 3 in experiment 3. The PCADP profiles were collected looking upstream in the direction of the channel centerline. While the initial current discharge, thickness, and excess density were the same for flows in both the straight and sinuous channels, the vertically averaged, streamwise velocity, $\bar{u}$, for flows in the straight channel were 1.6 times faster than flows in the high sinuosity channel (Fig. 12). This disparity between velocities in the straight and high sinuosity channels was corroborated by measurements of dye injected into turbidity currents and tracked with overhead photography. The velocity of the leading dye edge in the straight channel was 0.22 m/s compared to 0.13 m/s in the high sinuosity channel. The maximum streamwise current velocities in the straight channel were 1.7 times greater than values from the high sinuosity channel, similar to the velocity difference estimated from the velocity profiles. Analysis of the overhead video
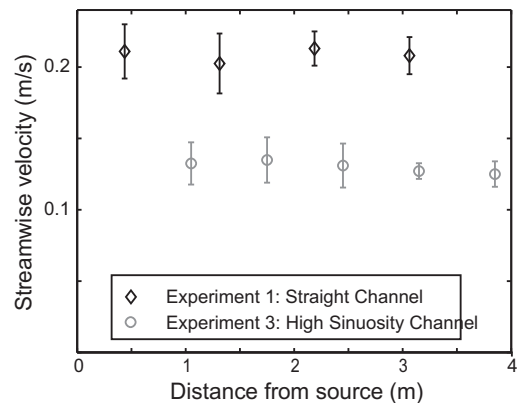

Fig. 12. Profiles of streamwise velocity in the straight channel experiment (black solid line) and high sinuosity channel experiment (gray dashed line) measured at the channel centerline, 2.95 m downstream from the channel entrance. Streamwise velocity measured with PCADP. Vertical error bars define the extent of each sampling volume while the horizontal error bars are +/− one standard deviation calculated using all values for current velocity in each sampling volume.

also showed that the mean streamwise velocity did not vary as a function of downstream distance in either channel (Fig. 13).

3.5. Suspended sediment concentration data

Profiles of suspended sediment concentration and grain size were collected during experiments 1 and 3 using a set of vertically stacked siphons positioned at 2.95 m from the channel entrance at its centerline; the same location where velocity profiles were collected (Fig. 12). In the straight channel the suspended sediment concentration measured 10 mm above the channel bed was 1.7% by weight. At this height the median particle size of suspended sediment was 28 μm. Concentration and median suspended particle size decreased with distance above the bed to 0.7% by weight and 18 μm at 50 mm (Fig. 14). In experiment 3 the suspended sediment concentration and median particle size measured 10 mm above the channel bed were 1.3% by weight and 25 μm; somewhat smaller than values measured at the same height in the straight channel. A slow decrease in suspended sediment concentration and median particle size with

Fig. 11. Cross-stream profiles of downstream velocity collected using PCADP for currents moving through the straight channel (A) and low sinuosity (B) channel experiments. Cross-section A is located 2.0 m from channel entrance, while cross-section B is located at the inflection point between bend 1 and 2 in the low sinuosity channel. Both cross-sections are oriented perpendicular to the local centerline direction and oriented looking downstream.

Fig. 13. Change in streamwise velocity as a function of distance from channel entrance measured along channel axis in the straight and high sinuosity channels. Streamwise velocity measured from dye injections into current body and captured using overhead digital video during 10 flow events in straight and high sinuosity channel experiments. Error bars represent +/− one standard deviation.
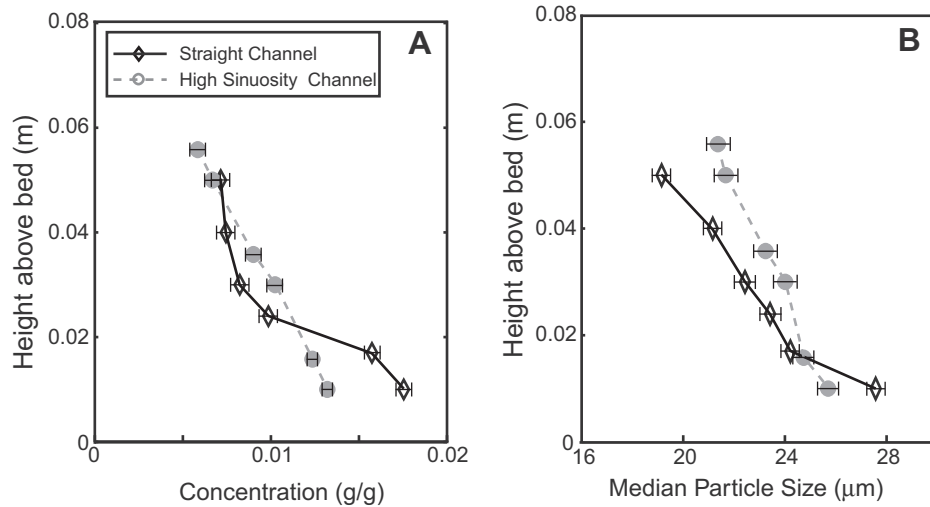
Fig. 14. Profiles of suspended sediment concentration and mean suspended particle size in the straight channel experiment (black solid line) and high sinuosity channel experiment (gray dashed line) measured at the channel centerline, 2.95 m downstream from the channel entrance. A) Profile of suspended sediment concentration. Data points represent average concentration measured from 600 mL sample. B) Profile of suspended sediment particle size. Data points represent median grain size measured from 600 mL sample.

increasing height into the flow was noted for this experiment relative to the straight channel case. Suspended sediment concentration and median particle size in the sinuous channel measured at 56 mm above the bed were 0.5% by weight and 21 μm (Fig. 14).

4. Interpretation

4.1. Containment of flows in sinuous channels

Reduced scale laboratory experiments performed by Straub et al. (2008) and Islam et al. (2008) have demonstrated that the inertia of turbidity currents in sinuous channels can lead to significant flow run-up on the outer banks of channel bends. Under what conditions is this run-up great enough for currents to completely exit channels and become unconfined flows? In order for a current to successfully traverse a sinuous channel, its streamlines must change direction at the apexes of bends or immediately downstream from them. This change in flow direction comes about through an interaction of flow with the outer bank of a bend. Our experiments show that this redirection of a current will not occur if the basal portion of a channelized flow has sufficient *KE* to run-up the height of the outer channel bank to the elevation of the confining levee crest. We therefore use a ratio of the kinetic energy for a current to the potential energy associated with the entire current leaving a channel to estimate the velocity at which a current will no longer be contained by topography:

$$\frac{KE}{PE} = \frac{1}{2}\frac{u^2}{\left(1 - \frac{\rho_a}{\rho_c}\right)gh} \leq 1 \qquad (6)$$

Eq. (6) can be rearranged to solve for U_{max}, the maximum velocity possible for flow to be partially contained within a channel, assuming a value for *KE/PE* of less than 1 is necessary for partial flow containment:

$$U_{max} \leq \sqrt{2gh\left(1 - \frac{\rho_a}{\rho_c}\right)} \qquad (7)$$

It is worth noting that Eq. (6) is similar in form to a densimetric Froude number. In a study of atmospheric flow interacting with a mountains, Snyder et al. (1985) proposed that flow with an internal densimetric Froude number greater than 1 could

completely surmount an obstacle rather than being partially to completely redirected by it. In a more recent review paper on the mechanics of turbidity currents, Kneller and Buckee (2000) suggested that a similar formulation defines the flow regime where turbidity currents have enough momentum to overcome seafloor obstacles such as sea mounts. Under conditions where ρ_c and ρ_a are roughly equal, estimates of velocity from Eq. (7) or a rearranged internal densimetric Froude number yield similar values. However when ρ_a is much less than ρ_c, U_{max} calculated with a rearranged internal densimetric Froude number diverges from values calculated with Eq. (7) toward unrealistically high values.

Fig. 8 presents data showing that the containment of currents within sinuous channels is very sensitive to the amplitudes of bends and their overall sinuosity. Why does the control of *KE/PE* on current containment appear to be strong in the high sinuosity channel experiment relative to the low sinuosity channel experiment? In their study of atmospheric flow interacting with mountains, Snyder et al. (1985) found that the internal densimetric Froude Number did not accurately predict flow–mountain interaction in those cases where flows approached the obstruction with a low attack angle. They concluded that a correction to their formulation was needed for attack angles less than 50°. In our experiments we define angle of attack as the angle between a line that is parallel to the channel centerline at the inflection point between two bends and a line that is parallel to the channel centerline at the bend apex (Fig. 15). With this definition the low sinuosity and high sinuosity channels had angles of attack equal to 19° and 57°, respectively. As a result it appears our experimental results are consistent with those of Snyder et al. (1985) and we conclude that Eq. (7) accurately predicts an upper limit for the streamwise velocities of turbidity currents traversing channels having one or more bends with attack angles greater than 50°. Observations of seafloor topography (Greene et al., 2002; Pirmez and Imran, 2003; Schwenk et al., 2003) indicate that this condition is satisfied by many submarine currents, suggesting that Eq. (7) can be used to estimate an upper bound on possible velocities for channel-forming turbidity currents.

4.2. Mixing of turbidity currents in channel bends

Laboratory studies of sediment transport phenomena associated with laterally confined turbidity currents have primarily been
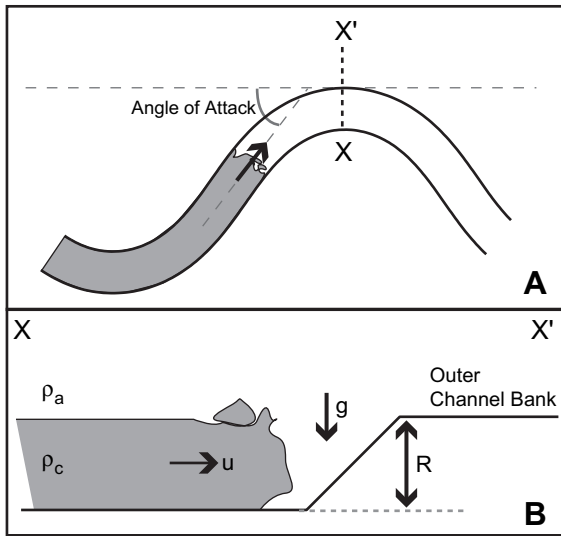
Fig. 15. Schematic illustration of channelized flows interacting with channel bends. A) Map view of the front of a channelized flow approaching a bend. Angle of attack is defined as the angle between a line that is parallel to the channel centerline at the inflection point between two bends and a line that is parallel to the channel centerline at the bend apex. B) Cross-section of channelized flow approaching the outer bank of a channel bend. Parameters which influence containment of the current include channel relief (h), gravity (g), current velocity (u), ambient fluid density (ρ_a), and current density (ρ_c).

carried out in straight channels (Garcia, 1994; Hallworth et al., 1993; Keevil et al., 2006; Middleton, 1966; Mohrig and Buttles, 2007; Straub et al., 2008). Of particular relevance to our study is the work of Dade and Huppert (1994) who calibrated a scaling relationship for the run-out distance of non-erosive turbidity currents using laboratory experiments performed in a straight channel. Dade and Huppert (1994) conclude that run-out distance, run-out time and characteristic deposit thickness all scale with the initial volume of suspended sediment, initial total volume of the current (sediment + liquid), and average settling velocity of the particles in suspension. Can channel sinuosity influence the run-out distance of currents? We address this question using data from experiments 1 and 3. The two channels constructed in these experiments had the same initial cross-sectional geometry so that we could isolate the control of channel sinuosity on the transport and deposition of suspended sediment.

Characteristic streamwise velocity profiles in Fig. 12 illustrate that currents moving through the straight channel of experiment 1 were 1.6 times faster than those moving though the highly sinuous channel of experiment 3. Since all other current properties were held constant the velocity ratio for currents in straight versus sinuous channels can be recast to determine the change in form drag, C_f, for channels of differing sinuosity using:

$$F_d = C_f \rho_c \frac{1}{2} \bar{u}^2 R_H L \tag{8}$$

where F_d is the drag force applied to the channel bed by the current, ρ_c is current density, R_H is hydraulic radius for the channel, and L is channel length. Using Eq. (8) we calculate that C_f is 2.1 times greater for the sinuous channel compared to straight form. This measured increase in C_f is similar to observations from rivers where the reported increase in drag associated with moving from straight to moderately sinuous channels is 1.5–1.8 (Chow, 1959; Cowan, 1956).

In both experiments 1 and 3 the bed topography was mapped following every current and differences between maps defined the net accumulation of sediment on the channel bed. Sedimentation associated with the first 10 currents released in both the straight

and highly sinuous channels is shown in Fig. 16a. Both centerline profiles in this figure show an approximately similar initial deposit thickness that decreases linearly with distance from the source. A greater amount of sediment deposition was measured along the channel centerline in the straight channel versus the sinuous one. This trend is also seen in Fig. 16b where integrated measures of deposit thickness from channel cross-sections are plotted as a function of distance from the channel entrance. Importantly, deposit thickness data summarized in Fig. 16b incorporates both the channelized and overbank deposits. As such, Fig. 16b also accounts for the sediment lost from currents on the proximal overbank surface. These results confirm that currents moving through the straight channel lost suspended sediment at higher rates than currents moving down the sinuous channel.

Measurements of velocity and deposit thickness present an interesting paradox: why are the slower moving currents traveling down the highly sinuous channel more effective at transporting a greater fraction of their suspended load through a channel segment than the faster, straight channel currents? This question has implications for determining the run-out distances of turbidity currents and since channels are built by the currents, it also has implications for the total lengths of submarine channels. Sediment loss from a current via deposition and entrainment of ambient water at the current's upper interface are the two primary mechanisms for decreasing a current's excess density, thereby limiting its run-out length (Hallworth et al., 1993; Parker et al., 1987). Velocity profiles measured at multiple downstream locations confirmed that water entrainment was negligible in both experiments (see Supplementary Information). Sediment deposition was therefore the dominant process controlling loss of excess density and current run-out lengths.

The profiles of suspended sediment concentration and median suspended particle size for currents in the straight and highly sinuous channels that are presented in Fig. 14 provide the information necessary to explain the observed differences in sediment deposition for the two channels. If bed-load is insignificant, the change in bed level can be estimated by the sediment-entrainment-deposition rate approach:

$$\Delta \eta_{bed} = \frac{(D - E)dt}{1 - \lambda} \tag{9}$$

where D and E respectively are sediment deposition and entrainment rates and λ is bed porosity (Garcia and Parker, 1993; Imran et al., 1998). Given that most entrainment rate formulations predict that entrainment scales with current velocity or near-bed shear stress (Garcia and Parker, 1993; Smith and McLean, 1977), both of which are higher for the straight channel experiments, the answer must lie in differences in the deposition rates for the two experiments. Deposition rate, D, can be approximated by:

$$D \sim C_{nb} w_s \tag{10}$$

where w_s is the settling velocity associated with the median grain size of the near-bed suspended sediment (Parker et al., 1987). We found that near-bed suspended sediment concentration, C_{nb}, and near-bed median grain size were both larger in the straight channel. As a result deposition was greater for the faster moving currents in the straight channel than those measured in the sinuous channel. We propose that a remixing of suspended sediment into the interior of currents at channel bends acts to reduce both C_{nb} and the mean diameter of particles transported close to the bed.

The experiments discussed here were designed to resolve channel topography through time and to connect this channel-form evolution to bulk properties of the depositional turbidity currents. Because of this only the most basic measures of the cross-
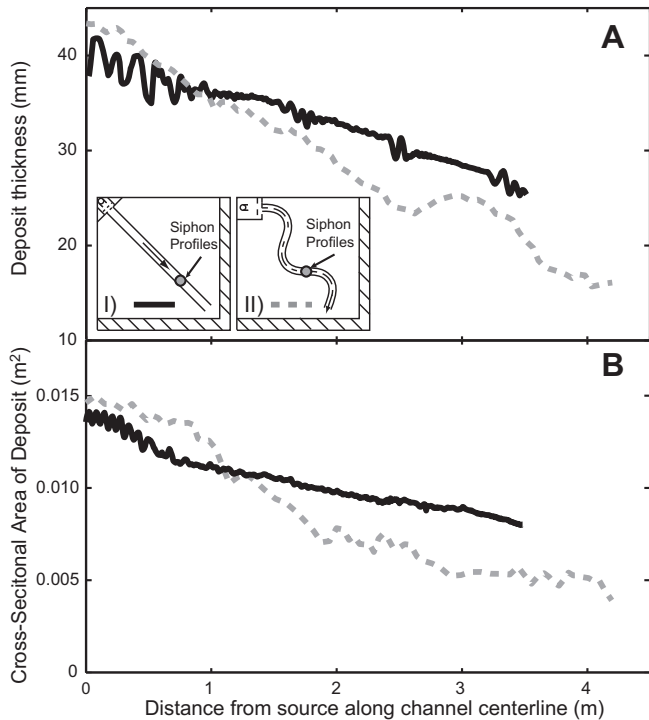
Fig. 16. A) Deposit thickness measured between the initial channel floor and deposit surface along the centerline of the straight (black solid line) and sinuous (gray dashed line) channel after 10 depositional flows. Straight channel profile is composed of 700 data points measured using a displacement laser at a spacing of 5 mm. Sinuous channel profile is composed of 92 data points measured with a 1 MHz ultrasonic transducer at a spacing of 40 mm. Inserts show the planform configuration for the I) straight and II) sinuous channel. Hatched pattern defines location of the basin moat. B) Vertical area of deposit measured along channel cross-sections oriented perpendicular to channel axis. Area measured between initial channel floor and deposit surface after 10 depositional flows.

stream structure to the flow and sediment transport fields were monitored here. Fortunately previous studies have resolved the influence of channel bends on the flow field and we apply information from these studies to the interpretation of the sediment-mixing process highlighted here. Straub et al. (2008) and Islam et al. (2008) found evidence for the run-up of turbidity currents onto the outer banks of channel bends in recent experimental studies. Overhead photography and properties of the resulting deposits revealed that the high-velocity core of the flow partially moved up and out of the channel at the outer banks at bends. We propose that the current run-up on the channel sidewalls aides wholesale current mixing at bends. The flow structure at channel bends has been measured in rivers (Thorne et al., 1985), and in laboratories using saline subaqueous density currents (Imran et al., 2007; Keevil et al., 2006). These studies resolved cross-stream velocities in bends and associated secondary flow cells with upward directed velocities. The laboratory measurements of (Keevil et al., 2006) also show enhanced turbulence intensities for density currents at channel bends compared to the straight channel crossings. All of these flow field observations are consistent with bed-induced remixing of the suspended sediment profile within turbidity currents.

4.3. Sedimentation in flow separation zones

Zones of low flow velocity were observed along sections of the inner banks of channel bends. These zones were imaged using both dye injections (Fig. 17) and series of PCADP profiles defining the velocity structure in channel cross-sections (Fig. 11B). Overhead

photography capturing dye intensity through time was particularly useful in delineating the low velocity zones in both the low and high sinuosity channels. In the low sinuosity channel each zone began just downstream from a bend apex along the inner channel bank and ended at the apex of the next channel bend. The bed of the channel and sedimentation patterns were measurably different in these low velocity zones compared to the adjacent active channel. Deposition rates were higher and ripples were absent from the channel bottom developing in these low velocity zones (Figs. 3 and 6). This sedimentation pattern produced bar forms that were attached to the inner banks of the low sinuosity channel.

The deposits that developed in the low velocity zones of the low sinuosity channel appear similar to oblique accretion deposits observed in bends of some rivers. Oblique accretion deposits are characterized by alternating sandy and muddy layers of sediment deposited from suspension (Page et al., 2003). These deposits are typically reported to form in zones of low velocity associated with the flow separating from the inner banks of bends (Brooks, 2003; Hickin, 1979; Smith et al., 2009). Suspended sediment is transported into these low velocity zones across a lateral shear zone that separates it from the core channel flow. Cross-sections of down channel velocity such as those presented in Fig. 11 reveal lateral gradients in velocity between the high-velocity core along the outer bank of channel bends and lower velocity flow along the inner channel bends. This lateral gradient in velocity induces mixing that transports sediment into the low velocity zone to build the bar. Fig. 7B,C clearly shows that sedimentation rates are highest immediately inboard from the separation line and diminish with distance toward the inner bank. We interpret this sedimentation pattern as the result of a progressive loss of suspended sediment from the fluid in the low velocity zone as it moves toward the bank. As a result of their formation via sedimentation from suspension, oblique accretion deposits have markedly different lateral and vertical continuity when compared to point bar deposits which are primarily formed through bed-load transport. Specifically, oblique accretion deposits are likely to be reworked less frequently than point bar deposits, preserving the original continuity of sedimentation units relative to point bars. The lack of ripples developed on the inner bank bars of our low sinuosity channel confirms that these deposits in these zones of separated flow were
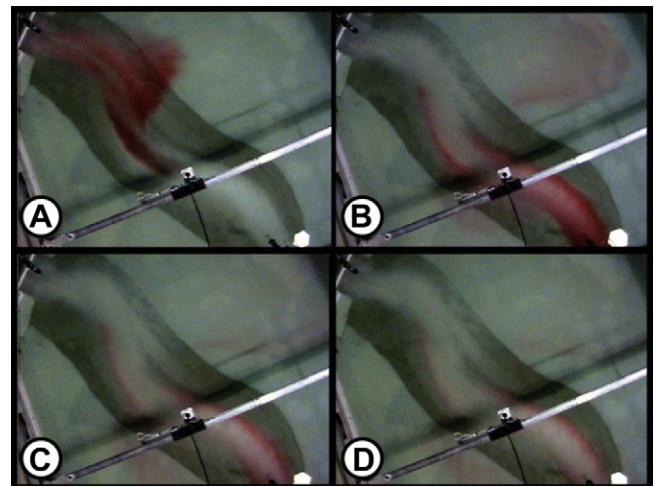
Fig. 17. Sequence of 4 images (A–D) separated by 30 s which help define separation zones immediately downstream of bends 1 and 2 in the low sinuosity experiment using time variation in tracer intensity recorded in overhead photos. Zones of flow separation developed along the inner channel banks downstream of each channel bend defined here by relatively low dye concentrations as dye plug initially passes downstream followed by relatively high dye concentrations later in the flow.

not significantly reworked by bed-load transport following sedimentation from suspension fallout.

The deposits that formed in the separation zones along the inner banks of the low sinuosity channel have geometries resembling those referred to as inner levees in several submarine channel systems (Deptuck et al., 2003) (Fig. 18). These inner levee deposits have been interpreted to form as a result of suspension fallout by overbanking flow associated with channels that are confined within larger canyon systems. The development of similar looking deposits within low velocity zones of channelized flow highlights a potential difficulty in separating oblique accretion bar forms from inner levee deposits when interpreting submarine channel fills. This separation is important for accurate paleo-environmental reconstructions because one is clearly linked to channelized processes while the other is linked to overbanking flow.

Low velocity zones were also observed in the high sinuosity channel. In this experiment these zones were situated along the inner banks of bends between their apexes to a position just downstream from the channel inflection point. Unlike the low sinuosity experiment, low velocity zones in the high sinuosity channel resulted in deposits that were consistently finer grained and thinner than deposits associated with the high-velocity core (Fig. 4). We propose that run-up of currents onto the outer banks of the high sinuosity channel laterally displaced the potential source of suspended sediment for separation zones to a degree that they were relatively starved of sediment. This increase in lateral displacement of the sediment-rich flow can be seen in Fig. 10 where the position of the high-velocity core for currents in the high sinuosity channel is located a greater lateral distance from the separation zones along its inner banks. Additional research is clearly required in order to fully determine the mechanisms controlling the transport of suspended sediment from the core flow into inner bank separation zones. In spite of this uncertainty we are confident that zones of flow separation are common in natural submarine channels and that accurate interpretation of deposits accumulated on the inner banks of bends requires considering the possibility that this sedimentation occurred in such zones of low current velocity.

5. Discussion

5.1. Constraining maximum flow velocity for channelized flows

Our experiments confirm that currents are unlikely to remain confined to developing channel forms with angles of attack greater than 50° when the kinetic energy of a flow exceeds the potential energy associated with an elevation gain equal to the channel relief.
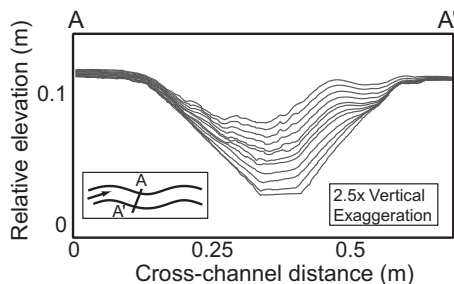
Fig. 18. Evolution of channel cross-sections located close to the channel inflection point located between the first and second channel bend. Figure displays the original channel form plus successive forms following sedimentation by two currents between the initial condition and post flow 26. Cross-section is oriented perpendicular to the local center-line direction and oriented looking downstream. Bar form located on the right-hand side of figure has similar morphology in cross-section to an inner levee, even though formative processes are different.

Channel bends with attack angles greater than 50° are commonly observed in the deep ocean and on other planets and moons (Bray et al., 2007; Perron et al., 2006; Schenk and Williams, 2004; Schwenk et al., 2003; Williams-Jones et al., 1998). We use Eq. (7) in conjunction with a range of values of ρ_c to estimate U_{max} for flows in submarine channels (Fig. 19A). We observe an initial rapid increase in U_{max} followed by a slower increase in U_{max} as channels increase in relief. As the value of ρ_c decreases a lower U_{max} is predicted for channels with a given depth.

Pirmez and Imran (2003) used several numerical methods to estimate a minimum turbidity current velocity of 1 m/s for channel-forming flows in the Amazon submarine channel at a position 400 km downstream from the shelf-edge. At this location the channel depth is ˜50 m and ρ_c was estimated to equal 1040 kg/ m^3 ± 20 kg/m^3 for channel-forming flows. Using Eq. (7) we estimate a U_{max} of 3.1 m/s. Eq. (7) and the methods of Pirmez and Imran (2003) define a narrow range of most likely velocity for channel-forming flows in the submarine Amazon channel.

Our results on conditions for flow containment are not limited to submarine channels, but can also be utilized in other environments where the ratio of ρ_c to ρ_a is small. As such we use Eq. (7) to estimate maximum channelized flow velocities on other planets and moons (Fig. 19B) using published values of g, ρ_c, and ρ_a in these settings (Table 3). Motivated by images of a possible channel network on the surface of Titan, Perron et al. (2006) utilized formulations for sediment transport conditions on Earth to estimate flow velocities on Titan. They assumed that formation of the channel network required the erosion of sediment from the landscape. Perron et al. calculated a U_{min} necessary to transport observed clasts with nominal diameters from 1 to 1000 mm. Their estimates ranged between 0.2 and 1.6 m/s depending on grain size. The Titan images show channels that are 1−30 m wide. Assuming a width to depth ratio of 10, a value similar to many rivers (Leopold and Wolman, 1960), we estimate a maximum channel depth of 3 m for the network imaged by the Huygens probe (Tomasko et al., 2005). Applying Eq. (7) we estimate a U_{max} of 2.8 m/s for this channel flow. Our estimate of U_{max} together with the Perron et al. (2006) estimate of U_{min} produce a surprisingly narrow window of most likely channel-forming flow velocities for the Titan system.

Given the remote location and infrequency of flow events in many recently discovered submarine channelized landscapes, in situ measurements of flow conditions will be limited in the near future. Methods to estimate flow conditions from channel morphology are necessary to characterize channel-forming environmental conditions. This is best done through development of methods that estimate minimum and maximum flow properties values necessary for channel development, such as the method for estimating U_{max} developed here.

5.2. How sinuosity can affect the total length of submarine channels

The laboratory study presented here illustrates how the presence of channel bends affects the rate of sediment loss from depositional turbidity currents. We propose that frequent remixing of the suspended sediment profile as a current moves through the many bends of a sinuous channel can act to significantly reduce rates of sediment loss via deposition from suspension fallout. In addition, this mechanism might be enhanced in field scale turbidity currents relative to our lab experiments where all of the excess density associated with a flow is provided through suspended sediment. In these field scale flows the production of density stratification between channel bends is likely to be greater than these experimental flows which had a fraction of their excess density supplied by dissolved salt that was well mixed vertically in the currents. The resulting maintenance of current density
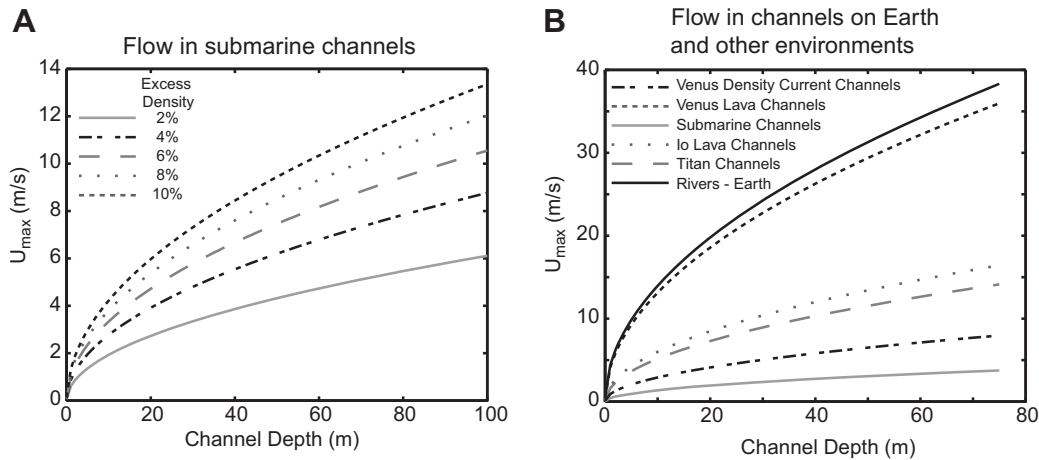
Fig. 19. (A) Estimates of U_{max} for turbidity currents in submarine channels between 0 and 100 m deep and with current excess densities ranging between 2 and 10%. (B) Estimates of U_{max} for flows in channels between 0 and 75 m deep for environmental conditions on Earth, Venus, Titan, and Io. Velocities are calculated using Eq. (7). Estimates for g, ρ_c, and ρ_a in these systems are taken from the published literature and summarized in Table 3.

combined with a repositioning of the center of suspended sediment mass at some level higher off of the channel bed would promote greater run-out distances for a current, providing both the current and sediment necessary for extending long submarine channels. The bend-induced sediment-mixing mechanism proposed here should also apply to erosive turbidity currents (Pantin, 2001). Use of a 3-D numerical model for density current flow down channels of arbitrary shape (Kassem and Imran, 2005) that explicitly includes sediment transport is necessary to test and refine our understanding of the role of topographically induced mixing on turbidity current run-out and channel construction. Even so, results presented here show that channelized run-out is not simply a function of initial current properties (Dade and Huppert, 1994), but is also influenced by the planform of the evolving channel itself. Moderate to highly sinuous channels promote the long-distance transport of sediment via turbidity currents into the deep-marine environment.

6. Summary

1) We released a sequence of turbidity currents into sinuous channels in an experimental basin filled with water and monitored current velocity at the channel entrance and exit in order to characterize the degree to which the currents remained containment within the channel forms. Flow containment is directly tied to channel formation because without it the patterns of sedimentation and erosion that lead to channel construction do not arise. Experimental observations confirm that a current is unlikely to remain confined to a developing channel form when the kinetic energy of a flow exceeds the potential energy associated with an elevation gain

equal to the channel relief. This balance of kinetic and potential energies allows us to constrain a maximum flow velocity that can be reasonably associated with a channel given limited knowledge of environmental conditions. This method can be used to constrain the maximum flow velocity for turbidity currents in sinuous submarine channels in addition to channels on Titan, Io, Venus.

2) Our laboratory experiments document the importance of channel bends in mixing suspended sediment within the interiors of turbidity currents. We found that current velocities, vertical suspended sediment profiles, and deposition rates vary in a straight vs. a moderately sinuous (1.32) channel. Vertical sediment concentration and grain size profiles collected at the centerline of each channel at the same downstream distance show greater vertical stratification of flow in the straight channel. This increased stratification lead to higher deposition rates at equivalent distances downstream in the straight channel relative to the sinuous channel. Vertical mixing caused by interactions of currents and channel bends helps sustain relatively high suspended sediment concentrations in current interiors, maintaining an excess density structure necessary to drive currents down slope. We hypothesize that a wholesale vertical mixing of currents induced by channel bends aides the long run-out turbidity currents and the construction long submarine channel systems.

3) Turbidity currents in our experiments separated from channel sidewalls along the inner banks of bends. In some cases, sedimentation rates and patterns within the resulting separation zones were sufficient to construct bar forms that were attached to the channel sidewalls. These bar forms have geometries that are similar to oblique accretion deposits which typically form in zones of low velocity associated with flow separation in rivers. These bar forms have inclined strata that might be mistaken for the deposits of point bars and internal levees.

Acknowledgements

Table 3
Environmental parameters used in calculation of U_{max} in Fig. 19.

	g (m/s^2)	ρ_c (kg/m^3)	ρ_a (kg/m^3)
Rivers–Earth	9.8	1000	1.2
Turbidity currents/Submarine channels	9.8	1040–1130	1030
Titan[a]	1.32	450	5.83
Io[b]	1.8	2650	2×10^{-7}
Venus Lava Channels[c]	8.9	2100	65
Venus Density Current Channels[d]	8.9	66–71	65

[a] Perron et al., 2006.
[b] Schenk and Williams, 2004.
[c] Williams-Jones et al., 1998.
[d] Bray et al., 2007.

Appendix. Supplementary information

Supplemental videos can be found at: http://www.tulane.edu/~kmstraub/Publications/Straub_TC_Experiments.wmv. Supplementary data associated with this article can be found, in the online version, at doi:10.1016/j.marpetgeo.2010.05.014.

References

Abreu, V., Sullivan, M., Pirmez, C., Mohrig, D., 2003. Lateral accretion packages (LAPs): an important reservoir element in deep water sinuous channels. Marine and Petroleum Geology 20, 631–648.

Anderson, A.G., 1941. Measurment and Analysis of Sediment Loads in Streams. St. Anthony Falls Laboratory, St. Paul, MN, pp. 99.

Babonneau, N., Savoye, B., Cremer, M., Klein, B., 2002. Morphology and architecture of the present canyon and channel system of the Zaire deep-sea fan. Marine and Petroleum Geology 19, 445–467.

Bouma, A., Normark, W.R., Barnes, N.E., 1985. Submarine Fans and Related Turbidite Systems. Springer Verlad, New York.

Bray, V.J., Bussey, D.B.J., Ghail, R.C., Jones, A.P., Pickering, K.T., 2007. Meander geometry of Venusian canali: constraints on flow regime and formation time. Journal of Geophysical Research 112, EO4S05. doi:10.1029/2006JE002785.

Brooks, G.R., 2003. Alluvial deposits of a mud-dominated stream: the Red River, Manitoba, Canada. Sedimentology 50, 441–458.

Chow, V.T., 1959. Open-channel Hydraulics. McGraw-Hill, New York, pp. 680.

Clark, J., Kenyon, N., Pickering, K., 1992. Quantitative analysis of the geometry of submarine channels: implications for the classification of submarine fans. Geology 20, 633–636.

Corney, R.K.T., Peakall, J., Parsons, D.R., Elliott, L., Amos, K.J., Best, J.L., Keevil, G.M., Ingram, D.B., 2006. The orientation of helical flow in curved channels. Sedimentology 53, 249–257.

Cowan, W.L., 1956. Estimating hydraulic roughness coefficients. Agricultural Engineering 37, 473–475.

Dade, W.D., Huppert, H.E., 1994. Predicting the geometry of channelized deep-sea turbidites. Geology 22, 645–648.

Das, H., Imran, J., Pirmez, C., Mohrig, D., 2004. Numerical modeling of flow and bed evolution in meandering submarine channels. Journal of Geophysical Research 109, 1–17.

Deitrich, W.E., 1982. Settling velocity of natural particles. Water Resources Research 18, 1615–1626.

Demyttenaere, R., Tromp, J.P., Ibrahim, A., Allman-Ward, P., Meckel, T., 2000. Brunei Deep Water Exploration: From Sea Floor Images and Shallow Seismic Analogues to Depositional Models in a Slope-Turbidite Setting. GCSEPM Foundation 20th Annual Research Conference, Deep-Water Reservoirs of the World, pp. 304–317.

Deptuck, M.E., Steffens, G.S., Barton, M., Pirmez, C., 2003. Architecture and evolution of upper fan channel-belts on the Niger Delta slope and in the Arabian Sea. Marine and Petroleum Geology 20, 649–676.

Droz, L., Rigaut, F., Cochonat, P., Tofani, R., 1996. Morphology and recent evolution of the Zaire turbidite systems (Gulf of Guinea). Geological Society of America Bulletin 108, 253–269.

Fildani, A., Hubbard, S.M., Romans, B.W., 2009. Stratigraphic Evolution of Deep-Water Architecture. In: Volume SEPM Field Trip Guidebook No. 10. SEPM.

Flint, S.S., Hodgson, D.M., Sprague, A.R., Brunt, R.L., Van der Merwe, W.C., Figueiredo, J., Prélat, A., Box, D., Di Celma, C., Kavanagh, J.P., 2011. Depositional Architecture And Sequence Stratigraphy Of The Karoo Basin Floor To Shelf Edge Succession, Laingsburg Depocentre, South Africa. Marine and Petroleum Geology 28, 658–674.

Flood, R.D., Damuth, J.E., 1987. Quantitative characteristics of sinuous distributary channels on the Amazon deep-sea fan. Geological Society of America Bulletin 98, 728–738.

Garcia, M.H., 1994. Depositional turbidity currents laden with poorly sorted sediment. Journal of Hydraulic Engineering 120, 1240–1263.

Garcia, M.H., Parker, G., 1993. Experiments on the entrainment of sediment into suspension by a dense bottom current. Journal of Geophysical Research 98, 4793–4807.

Graf, W.H., 1971. Hydraulics of Sediment Transport. McGraw-Hill, New York, pp. 513.

Greene, H.G., Maher, N.M., Paull, C.K., 2002. Physiography of the Monterey Bay National Marine Santuary and implications about continental margin development. Marine Geology 181, 55–82.

Hallworth, M.A., Phillips, J.C., Huppert, H.E., Sparks, R.S., 1993. Entrainment in turbulent gravity currents. Nature 362, 829–831.

Hickin, E.J., 1979. Concave-bank benches on the Squamish River, British Columbia. Canadian Journal of Earth Sciences 16, 200–203.

Howard, A.D., 1980. Thresholds in river regimes. In: Coates, D.R., Vitek, J.D. (Eds.), Thresholds in Geomorphology. Allen and Unwin, Concord, Massachusetts, pp. 227–258.

Imran, J., Islam, M.A., Huang, H., Kassem, A., Dickerson, J., Pirmez, C., Parker, G., 2007. Helical flow couplets in submarine gravity underflows. Geology 35, 659–662.

Imran, J., Parker, G., Katopodes, N., 1998. A numerical model of channel inception on submarine fans. Journal of Geophysical Research 103, 1219–1238.

Imran, J., Parker, G., Pirmez, C., 1999. A non-linear model of flow in meandering submarine and subaerial channels. Journal of Fluid Mechanics 400, 295–331.

Islam, M.A., Imran, J., Pirmez, C., Cantelli, A., 2008. Flow splitting modifies the helical motion in submarine channels. Geophysical Research Letters 35.

Kane, I.A., Hodgson, D.M., 2011. Sedimentological criteria to differentiate submarine channel levee subenvironments: exhumed examples from the Rosario Fm. (Upper Cretaceous) of Baja California, Mexico, and the Fort Brown F. (Permian), Karoo Basin, S. Africa. Marine and Petroleum Geology 28, 807–823.

Kane, I.A., McCaffrey, W., Peakall, J., 2008. Controls on sinuosity evolution within submarine channels. Geology 36, 287–290.

Kassem, A., Imran, J., 2005. Three-dimensional modeling of density current. II. Flow in sinuous confined and unconfined channels. Journal of Hydraulic Research 42, 591–602.

Keevil, G.M., Peakall, J., Best, J.L., Amos, K.J., 2006. Flow structure in sinuous submarine channels: velocity and turbulence structure of an experimental submarine channel. Marine Geology 229, 241–257.

Kenyon, N., Amir, A., Cramp, A., 1995. In: Pickering, K., Hiscott, R.N., Kenyon, N., Ricci Lucchi, F., Smith, R.D.A. (Eds.), Atlas of Deep Water Environments: Architectural Style in Turbidite Systems. Chapman and Hall, London, pp. 89–93.

Kneller, B., 2003. The influence of flow parameters on turbidite slope channel architecture. Marine and Petroleum Geology 20, 901–910.

Kneller, B., Buckee, C.M., 2000. The structure and fluid mechanics of turbidity currents: a review of some recent studies and their geological implications. Sedimentology 47, 62–94.

Komar, P.D., 1969. The channelized flow of turbidity currents with application to Monterey deep-sea fan channel. Journal of Geophysical Research 74, 4544–4558.

Langbein, W., Leopold, L., 1966. River meanders and the theory of minimum variance. In: Dury, G.H. (Ed.), Rivers and River Terraces, pp. 238–263.

Leopold, L.B., Wolman, M.G., 1960. River meanders. Geological Society of America Bulletin 71, 769–793.

Mackin, J.H., 1948. Concept of the graded river. Geological Society of America Bulletin 59, 463–512.

McHargue, et al., Architecture of turbidite channel systems on the continental slope: patterns and predictions, in this issue.

Metivier, F., Lajeunesse, E., Cacas, M.C., 2005. Submarine canyons in the bathtub. Journal of Sedimentary Research 75, 6–11.

Middleton, G., 1966. Experiments on density and turbidity currents I. Motion of the head. Canadian Journal of Earth Sciences 3, 523–546.

Mohrig, D., Buttles, J., 2007. Shallow channels constructed by deep turbidity currents. Geology 35, 155–158.

Nakajima, T., Peakall, J., McCaffrey, W.D., Paton, D.A., Thompson, P.J.P., 2009. Outer-bank bars: a new intra-channel architectural element within sinuous submarine slope channels. Journal of Sedimentary Research 79, 872–886.

Page, K.J., Nanson, G.C., Frazier, P.S., 2003. Floodplain formation and sediment stratigraphy resulting from oblique accretion on the Murrumbidgee River, Australia. Journal of Sedimentary Research 73, 5–14.

Pantin, H.M., 2001. Experimental evidence for autosuspension. In: McCaffrey, W.D., Kneller, B., Peakall, J. (Eds.), Particulate Gravity Currents. Blackwell Science, Oxford, pp. 189–205.

Parker, G., Garcia, M.H., Fukushima, Y., Yu, W., 1987. Experiments on turbidity currents over an erodible bed. Journal of Hydraulic Research 25, 123–147.

Parsons, J.D., Garcia, M.H., 1998. Similarity of gravity current fronts. Physics of Fluids 10, 3209–3213.

Peakall, J., Amos, K.J., Keevil, G.M., Bradbury, P.W., Gupta, S., 2007. Flow processes and sedimentation in submarine channel bends. Marine and Petroleum Geology 24, 470–486.

Peakall, J., McCaffrey, B., Kneller, B., 2000. A process model for the evolution, morphology, and architecture of sinuous submarine channels. Journal of Sedimentary Research 70, 434–448.

Perron, J.T., Lamb, M.P., Koven, C.D., Fung, I.Y., Yager, E., Adamkovics, M., 2006. Valley formation and methane precipitation rates on Titan. Journal of Geophysical Research 111. doi:10.1029/2005JE002602.

Pirmez, C., 1994. Growth of a Submarine Meandering Channel-Levee System on the Amazon Fan. Columbia University.

Pirmez, C., Beaubouef, R.T., Friedmann, S.J., Mohrig, D., 2000. Equilibrium profile and baselevel in submarine channels: examples from Late Pleistocene systems and implications for the architecture of deepwater reservoirs. GCSEPM Foundation 20th Annual Research Conference, Deep-Water Reservoirs of the World, p. 782–805.

Pirmez, C., Imran, J., 2003. Reconstruction of turbidity currents in Amazon Channel. Marine and Petroleum Geology 20, 823–849.

Pratson, L., Ryan, W.B.F., Mountain, G.S., Twitchell, D.C., 1994. Submarine canyon initiation by downslope-eroding sediment flows: evidence in late Cenozoic strata on the New Jersey continental slope. Geological Society of America Bulletin 106, 395–412.

Pyles, D.R., 2008. Multiscale stratigraphic analysis of a structurally confined submarine fan: Carboniferous Ross Sandstone, Ireland. American Association of Petroleum Geologists Bulletin 92, 557–587.

Romans, B.W., Fildani, A., Hubbard, S.M., Covault, J.A., Fosdick, J.C., Graham, S.A., 2011. Evolution Of Deep-Water Stratigraphic Architecture, Magallanes Basin, Chile. Marine and Petroleum Geology 28, 612–628.

Schenk, P.M., Williams, D.A., 2004. A potential thermal erosion lava channel on Io. Geophysical Research Letters 31, L23702. doi:10.1029/2004GL021378.

Schwenk, T., Speiss, V., Hubscher, C., Breitzke, M., 2003. Frequent channel avulsions within the active channel-levee system of the middle Bengal fan – an exceptional channel-levee development derived from Parasound and Hydrosweep data. Deep-Sea Research II 50, 1023–1045.

Simpson, J.E., 1987. Gravity Currents in the Environment and the Laboratory. Ellis Horwood, Chichester, England, pp. 244.

Smith, D.G., Hubbard, S.M., Leckie, D.A., Fustic, M., 2009. Counter point bar deposits: lithofacies and reservoir significance in the meandering modern Peace River and ancient McMurray Formation, Alberta, Canada. Sedimentology 56, 1655–1669.

Smith, J.D., McLean, S.R., 1977. Spatially averaged flow over a wavy surface. Journal of Geophysical Research 82, 1735–1746.

Snyder, W.H., Thompson, R.S., Eskridge, R.E., Lawson, R.E., Castro, I.P., Lee, J.T., Hunt, J.C.R., Ogawa, Y., 1985. The structure of strongly stratified flow over hills: dividing-streamline concept. Journal of Fluid Mechanics 152, 249–288.

Straub, K.M., Mohrig, D., McElroy, B., Buttles, J., Pirmez, C., 2008. Interactions between turbidity currents and topography in aggrading sinuous submarine channels: a laboratory study. Geological Society of America Bulletin 120, 368–385.

Sylvester, Z., Pirmez, C., Cantelli, A., 2011. A model of submarine channel-levee evolution based on channel trajectories: Implications for stratigraphic architecture. Marine and Petroleum Geology 28, 716–727.

Thorne, C.R., Zevengergen, L.W., Pitlick, J.C., Rais, S., Bradley, J.B., Julien, P.Y., 1985. Direct measurements of secondary currents in a meandering sand-bed river. Nature 315, 746–747.

Tomasko, M.G., Archinal, B., Becker, T., Bezard, B., Bushroe, M., Combes, M., Cook, D., Coustenis, A., de Bergh, C., Dafoe, L.E., Doose, L., Doute, S., Eibl, A., Engel, S., Gliem, F., Grieger, B., Holso, K., Howington-Kraus, E., Karkoschka, E., Keller, H.U., Kirk, R., Kramm, R., Kuppers, M., Lanagan, P., Lellouch, E., Lemmon, M., Lunine, J., McFarlane, E., Moores, J., Prout, G.M., Rizk, B., Rosiek, M., Rueffer, P., Schroder, S.E., Schmitt, B., See, C., Smith, P., Soderblom, L., Thomas, N., West, R., 2005. Rain, winds, and haze during the Huygens probe's descent to Titan's surface. Nature 438, 765–778.

Weimer, P., Link, M.H., 1991. In: Weimer, P., Link, M.H. (Eds.), Seismic Facies and Sedimentary Process of Submarine Fans of Submarine Systems. Sringer-Verlag, New York, pp. 9–67.

Williams-Jones, G., Williams-Jones, A.E., Stix, J., 1998. The nature and origin of Venusian canali. Journal of Geophysical Research 103, 8545–8555.